

Longitudinal emittance growth due to nonlinear space charge effect

Y. Y. Lau

The Chinese University of Hong Kong, Hong Kong

Simon S. Yu

*The Chinese University of Hong Kong, Hong Kong,
and Lawrence Berkeley National Laboratory, Berkeley, California 94720, USA*

John J. Barnard

Lawrence Berkeley National Laboratory, Berkeley, California 94720, USA

Peter A. Seidl

Lawrence Livermore National Laboratory, Livermore, California 94550, USA
(Received 15 April 2011; published 19 March 2012)

Emittance poses limits on the key requirements of final pulse length and spot size on target in heavy ion fusion drivers. In this paper, we show studies on the effect of nonlinear space charge on longitudinal emittance growth in the drift compression section. We perform simulations, using the 3D PIC code WARP, for a high current beam under conditions of bends and longitudinal compression. The linear growth rate for longitudinal emittance turns out to depend only on the peak line charge density, and is independent of pulse length, velocity tilt, and/or the pipe and beam size. This surprisingly simple result is confirmed by simulations and analytic calculations.

DOI: [10.1103/PhysRevSTAB.15.033501](https://doi.org/10.1103/PhysRevSTAB.15.033501)

PACS numbers: 52.58.Hm, 29.27.Eg, 41.75.Ak

I. INTRODUCTION

Heavy ion fusion driver designs require, in general, multiple intense ion beams with small spots and short durations to impinge on the target with precise timing. To generate the illumination pattern required by the target design, multiple drift compression beam lines with bends are usually required to transport beams from the multibeam linear accelerators to the target. For two-sided or one-sided indirect target designs, the final focusing magnets for each beam subtend a finite solid angle and area near the entrance to the reactor chamber. Since there are many such beams, packing considerations force some beams to be aimed at the target at significant angles, for example at about 20 degrees, relative to the polar axis of the group of beams. Direct targets require spherically symmetric beam configurations, implying yet larger angles of incidence at chamber entrance.

The pulse length and focal spot sizes at target are fundamentally limited by beam emittances just before the focus. How the beam dynamics within the final compression beam line affect the final emittances therefore becomes a crucial question. In the presence of bends, the transverse dynamics is greatly affected by longitudinal momentum dispersion. One source of momentum spread comes from the

head-to-tail velocity tilt required for beam compression, which will lead to centroid offset [1]. Another is the local velocity spread, which will also contribute to transverse emittance growth. Both the local velocity spread as well as head-to-tail distortion of the longitudinal phase space can lead to longitudinal emittance growth. Understanding the longitudinal emittance growth and finding ways of minimizing it, is the primary focus of this paper.

In this study, simulations are carried out to understand the origin and parametric dependence of the emittance growth, using WARP, a 3-dimensional particle-in-cell code designed especially for simulating high intensity heavy ion beams [2]. The results are compared to an analytic model using an approximation to the problem of the longitudinal space charge self-field of an intense, long beam (“g-factor” model) [3–5].

II. SIMULATION PARAMETERS AND RESULTS ON FINAL BEAM DIMENSIONS

In this paper, we use an example of a direct target, because the requirement on spherical symmetry is more demanding on the drift compression beam line design. The example we consider is a 1 MJ driver with 128 beams of 500 MeV rubidium+1 ions [6]. Beams are in a 4 polar ring configuration (Fig. 1). In a previous study, it was shown that this configuration could achieve sufficient uniformity for a direct target [7]. Because the beam channels are arranged in an annular symmetric configuration with beams entering from both sides, this essentially only

Published by the American Physical Society under the terms of the Creative Commons Attribution 3.0 License. Further distribution of this work must maintain attribution to the author(s) and the published article's title, journal citation, and DOI.

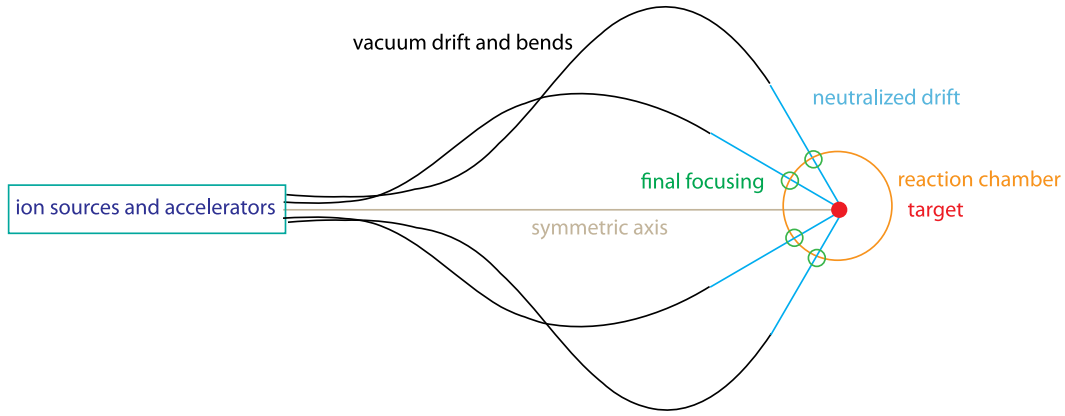


FIG. 1. Overview of beam channels geometry. The opposite side (which is not shown here) is identical.

requires 2 independent channel designs. In this study, we consider only the channel design for the smaller angle. Each channel consists of bends, a matching section, a plasma-filled neutralized drift [8], and final focusing section. The pipe is perfectly conductive with a uniform radius 10 cm to allow space for beams going through bends without hitting the wall. The bending section of each channel is made of two arcs arranged in opposite directions, adding up to a net of about 37 degrees of bend. The bending dipoles are in combined-function magnets with the confining quadrupoles, each 0.8 m long and the lattice period is 2 m. After the bends end there is a matching section, which consists of the last four quadrupoles just before the start of neutralization. They change the beam envelope to circular and slightly diverging when it enters the neutralized drift, allowing the beam to expand before the final focusing magnets. The length of the neutralized drift is about 27 m, in which the 12 T final focus solenoid is placed at 4 m before the target, close to the limit posed by

typical chamber size and neutron induced damage. The total length of the whole compression section is about 91 m, which is reasonable for cost and engineering issues. Table I lists some parameters used.

The effect of emittance on the final spot size and pulse length is shown by two main runs: one with canonical parameters as shown in Table I, and another with the same parameters, except for the initial emittances which are set to zero in all directions. The latter case corresponds to the most optimistic results for spot size and pulse length achievable under these conditions. The beam has semi-Gaussian distribution and a parabolic current profile, loaded with matched envelope in the lattice and given a linear head-to-tail velocity tilt for compression.

We first consider canonical parameters. As the beam runs along the channel, its dimensions are recorded as a function of z (Figs. 2 and 3). In particular, at the focus around $z = 91$ m, the final pulse length (twice rms) is about 4.8 ns and the spot size is about 5 mm on the target.

TABLE I. Parameters used in this study.

Parameter	Value
Initial peak current/beam (A)	100.0
Energy/beam (kJ)	7.5
Initial perveance	5.35×10^{-5}
Initial pulse length, rms (ns)	51
Initial transverse emittance (mrad)	5.2×10^{-5}
Initial longitudinal emittance (mrad)	4.56×10^{-3}
Velocity tilt	10%
Section total length (m)	91
Bend length (m)	20, 30
Neutralized drift length (m)	27
Lattice period (m)	2.0
Quad length (m)	0.8
Quad strength (T/m)	64.33
Maximum dipole strength (T)	4.65
Undepressed tune (degree)	72
Pipe radius (cm)	10

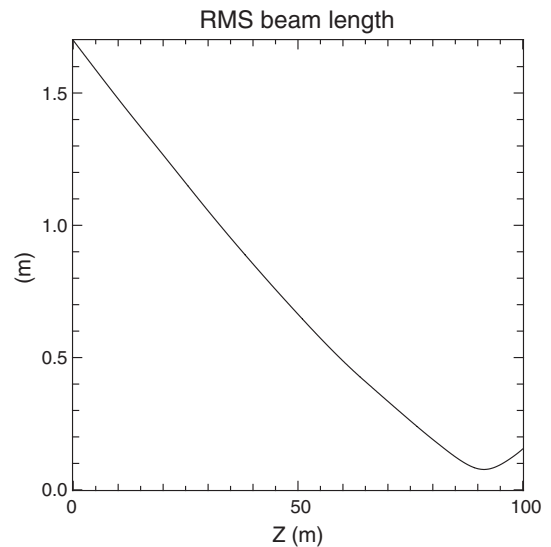


FIG. 2. Beam length as a function of z .

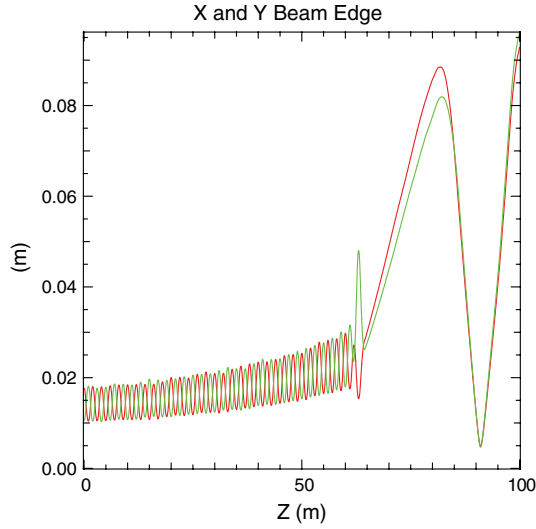


FIG. 3. Beam envelope (twice rms) as a function of z (red is x and green is y).

Next for the case with no initial emittance, the pulse length is 1.2 ns and a spot of roughly 2.6 mm, where ϵ_z and ϵ_x just before the focus are approximately 1.2×10^{-3} m rad and 3.5×10^{-5} m rad, respectively. These values are minimum achievable with the set of parameter used. To understand the physical origin of this emittance growth, we vary the input parameters, and observe the parametric dependence of the growth rate. The findings will be discussed in the next sections.

The final focused spot size is roughly given by transverse emittance divided by the final focus angle provided by final focus magnet a' [9]:

$$a_{\text{final}} \approx \frac{\epsilon_x}{|a'|}. \tag{1}$$

A similar expression can be derived for the pulse length observing the similarities between transverse and longitudinal envelope equations in the force-free region [10]. Here $|L'|$ is identified as beam velocity multiplied by final velocity tilt at the start of force-free region f :

$$L_{\text{final}} \approx \frac{\epsilon_z}{|L'|} = \frac{\epsilon_z}{v_b f}. \tag{2}$$

In addition, possible contributing factors other than emittance to the final spot size are remaining centroid offset, chromatic effects from off-momentum slices, and residual space charge effects. In the simulations, however, we observe those contributions from off-momentum slices are small. From Fig. 4 consider only the central slice (shown with blue line). Its spot is not much smaller than that of the whole beam, showing that the major limiting factor is still emittance.

III. EFFECT OF INITIAL EMITTANCE AND BENDS ON FINAL EMITTANCE

In reality, drift compression begins at the exit of the accelerator, where the beams come out with nonzero emittance. In this section, the final emittance given a range of input transverse and longitudinal emittances, will be discussed. The final emittance is recorded at the end of the bend section ($z = 60$ m), as we only focus on the growth within vacuum drift and bends, ignoring that in the matching and final focusing. Figure 5 shows a sample simulation run of emittance as a function of distance traveled. The

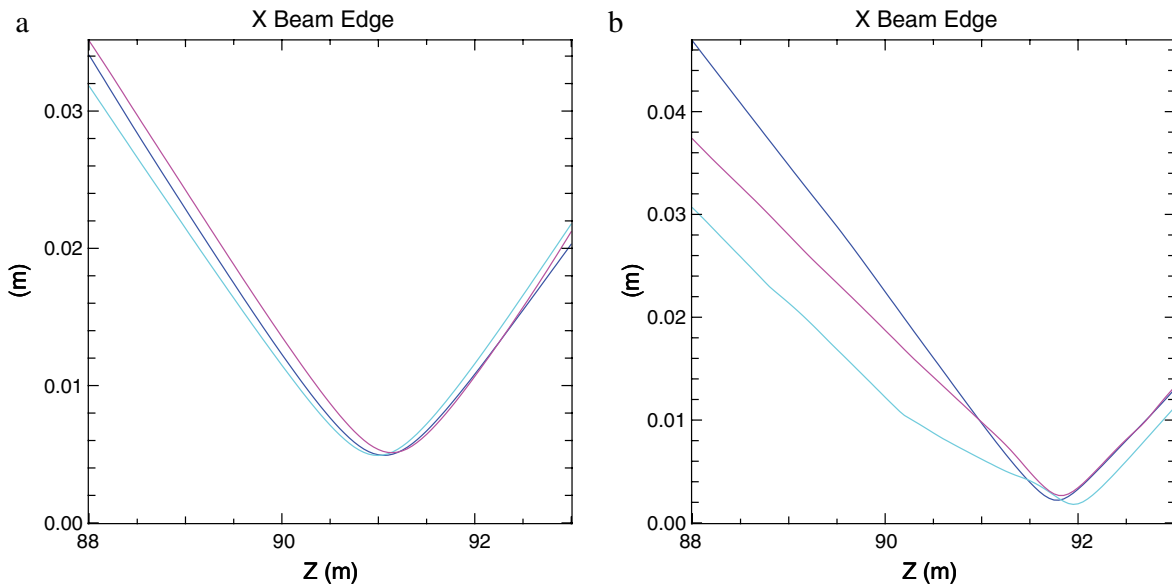


FIG. 4. Beam edge as a function of z near the focus showing a small chromatic effect: blue line corresponds to central slice; purple and cyan lines are off momentum slices near the beam tail and head, respectively. Two cases shown here are with normal emittance (a) and zero initial emittance (b).

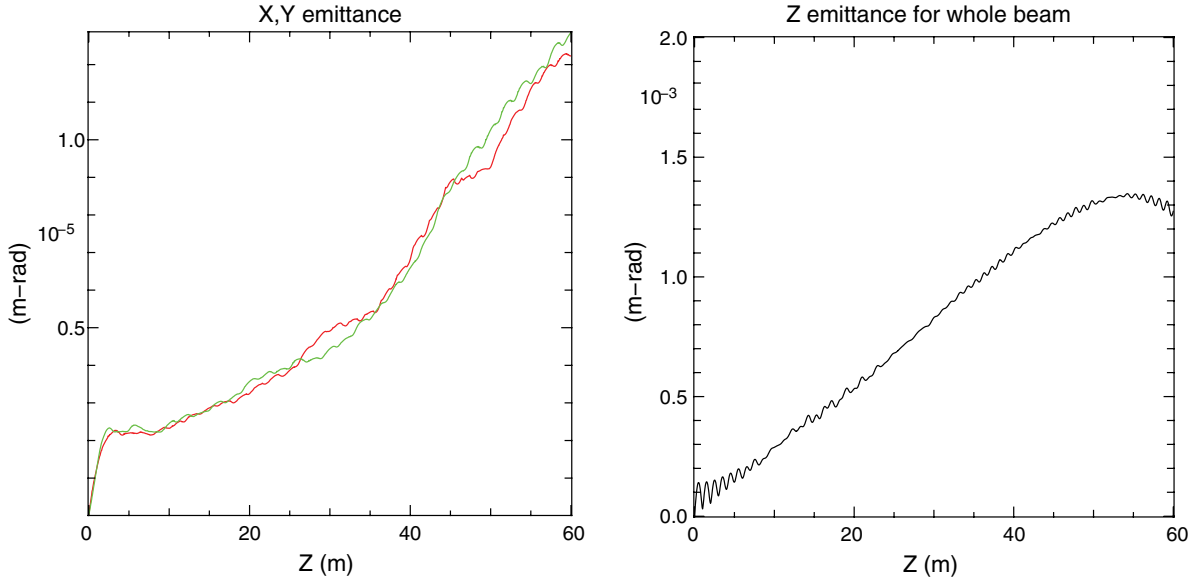


FIG. 5. One example of central slice x (red), y (green) emittances vs z and whole beam z emittance vs z ; all emittances are initially zero.

results of all runs are summarized in Figs. 6 and 7, respectively, for cases with bends and just a straight channel of the same length.

The square of the longitudinal emittance is defined in general as

$$\epsilon_z^2 = \frac{16}{v_b^2} [\langle (\Delta z)^2 \rangle \langle (\Delta v_z)^2 \rangle - \langle \Delta z \Delta v_z \rangle^2]. \quad (3)$$

Here v_b is the average beam velocity, Δz and Δv_z are the position and velocity difference from their respective means.

In our simulation, the initial emittance is assumed to be purely thermal, with $\Delta v_z = \delta v_t$ which is uncorrelated with Δz ($\langle \delta v_t \Delta z \rangle = 0$). The initial thermal emittance is then given by

$$\epsilon_t^2 = \frac{16}{v_b^2} \langle (\Delta z)^2 \rangle \langle \delta v_t^2 \rangle. \quad (4)$$

We observed an emittance growth which arises from a new component δv_c which may or may not be correlated with Δz . The square of the emittance may then be written

$$\epsilon_z^2 = \frac{16}{v_b^2} [\langle (\Delta z)^2 \rangle \langle (\delta v_t + \delta v_c)^2 \rangle - \langle \Delta z (\delta v_t + \delta v_c) \rangle^2] \quad (5)$$

$$\begin{aligned} \epsilon_z^2 = \frac{16}{v_b^2} [\langle (\Delta z)^2 \rangle (\langle \delta v_t^2 \rangle + \langle \delta v_c^2 \rangle + 2\langle \delta v_t \delta v_c \rangle) - \langle \Delta z \delta v_t \rangle^2 \\ - \langle \Delta z \delta v_c \rangle^2 - 2\langle \Delta z \delta v_t \rangle \langle \Delta z \delta v_c \rangle]. \end{aligned} \quad (6)$$

Now if δv_c and δv_t are uncorrelated, i.e. $\langle \delta v_t \delta v_c \rangle = 0$, then

$$\epsilon_z^2 = \epsilon_t^2 + \epsilon_c^2, \quad (7)$$

where $\epsilon_c^2 = \frac{16}{v_b^2} [\langle (\Delta z)^2 \rangle \langle \delta v_c^2 \rangle - \langle \Delta z \delta v_c \rangle^2]$. We define $\Delta \epsilon_z^2$ as the change in the square of the emittance,

$$\epsilon_{zf}^2 = \epsilon_{zi}^2 + \Delta \epsilon_z^2. \quad (8)$$

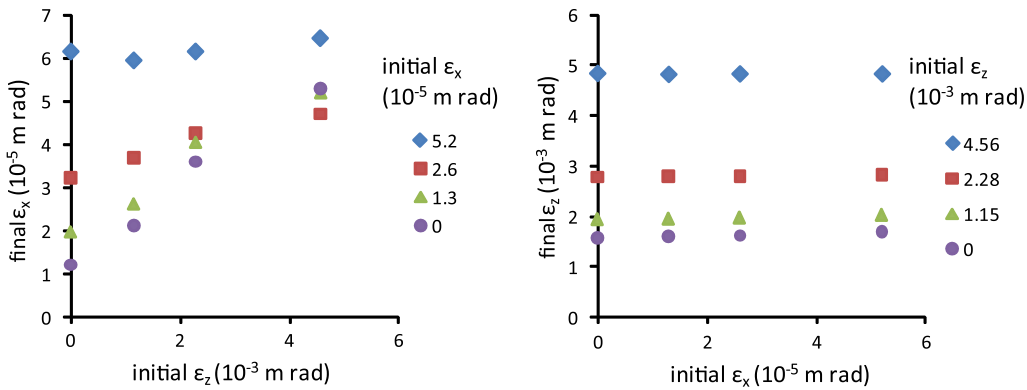


FIG. 6. Final emittance (x and z) vs initial emittance (x and z).

If the emittance growth and the assumed initial thermal spread are uncorrelated, then, as discussed above, we expect $\Delta\epsilon_z^2$ to be independent of the initial emittance ϵ_{zi} . Figures 8 and 9 demonstrate that this is indeed the case. Indeed, $\Delta\epsilon_z^2$ is also independent of ϵ_{xi} and no matter if bends are present.

On the other hand, if we treat transverse emittance similar to the above, we observe $\Delta\epsilon_x^2$ depends on ϵ_{xi} and especially

ϵ_{zi} when bends are present (Fig. 8). This means $\Delta\epsilon_x^2$ is correlated to the initial thermal distribution. However, the correlation is much weaker without bends (Fig. 9), suggesting momentum dispersion is a possible mechanism of correlation as particles within a slice traveling at different curvatures through the bends corresponding to their longitudinal momentum (see Refs. [1,11]). Hence, the thermal ϵ_{zi} directly affects $\Delta\epsilon_x^2$ in the direction of the bends.

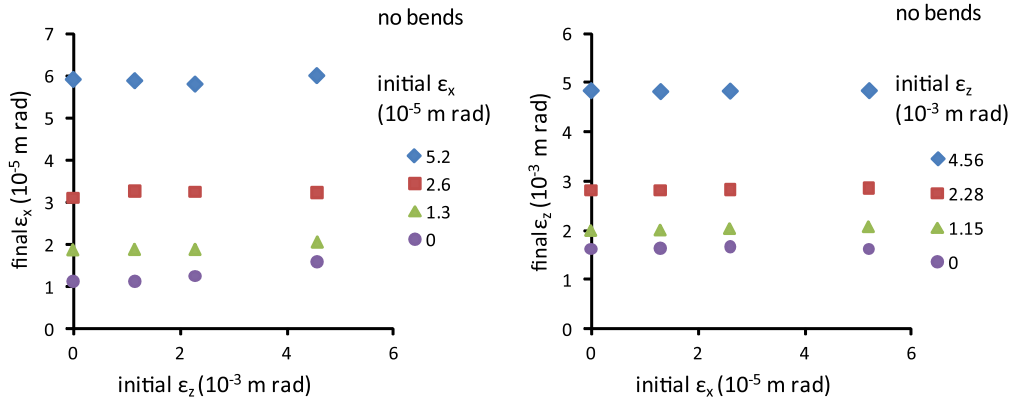


FIG. 7. Final emittance (x and z) vs initial emittance (x and z), runs with bends removed.

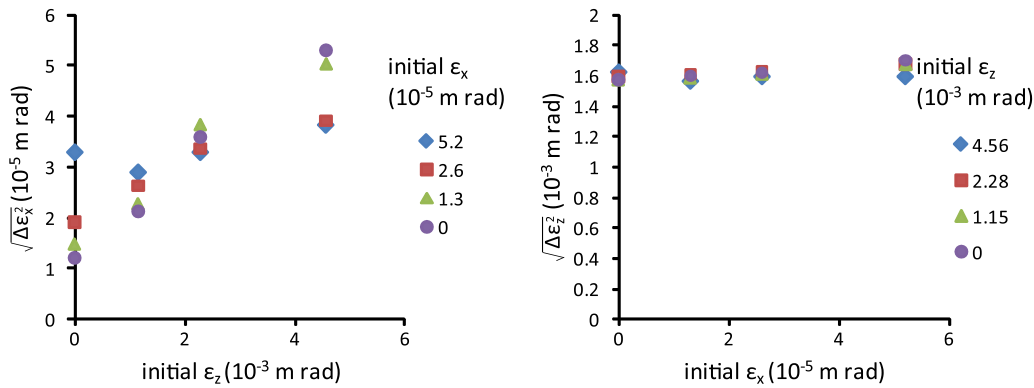


FIG. 8. Square root of $\Delta\epsilon_x^2$ and $\Delta\epsilon_z^2$ vs initial ϵ_x and ϵ_z .

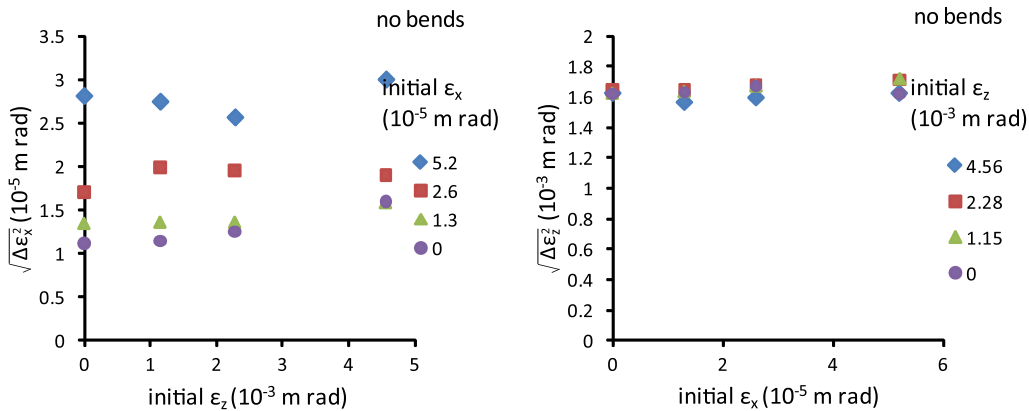


FIG. 9. Square root of $\Delta\epsilon_x^2$ and $\Delta\epsilon_z^2$ vs initial ϵ_x and ϵ_z , runs with bends removed.

The fact $\Delta\epsilon_z^2$ are essentially constant suggests it may be dominated by a single mechanism (in this case, the longitudinal space charge effect), which will be addressed in the next section.

IV. SPACE CHARGE EFFECT ON LONGITUDINAL EMITTANCE GROWTH

To understand the mechanism for longitudinal emittance growth in more detail, we carried out simulations of an initially cold beam with varying beam parameters. We consider a cold beam (i.e., zero emittance) as it provides the lower bounds for the final emittance and bunch length on target. In addition, previously presented results show the rate of longitudinal emittance growth is totally independent of the initial emittances assumed, thus it is sufficient to consider starting with zero emittance here. It provides an unambiguous scenario for the study of the physical mechanism for the emittance growth. Since we suspect that emittance growth is due to nonlinear space charge effect, the parameters we varied are related to the longitudinal space charge force. From the geometric factor model,

$$E_z = -\frac{g}{4\pi\epsilon_0} \frac{\partial\lambda}{\partial z}. \tag{9}$$

For an elliptical beam with radius independent of z and on axis,

$$g = \ln\left(\frac{R_p^2}{ab}\right) + 1, \tag{10}$$

where R_p denotes pipe radius, and a and b are envelope in x and y directions.

The parameters we vary include the geometric factor and peak current; these appear explicitly and scale directly with longitudinal electric force of the beam. In addition, we also vary the beam length and velocity tilt, both of which would affect the rate at which the beam compresses.

Starting with the canonical parameters: 100 A current, 200 ns pulse length, and 10% velocity tilt, one parameter is varied each time. In all runs, longitudinal emittance growth follows the pattern exhibited in Fig. 8, which can be summarized as follows: an initial nearly linear growth followed by a slight acceleration in the growth rate and, finally, the growth slows down, peaks at a certain value, and drops back. Depending on the initial beam parameters, the relative position in z for the transition from the linear to nonlinear phase varies.

In Figs. 10–13, we summarize the final emittance at the position of 60 m. In Fig. 10, we vary the geometric factor; this is done by changing the pipe radius (10, 8, and 5 cm) and/or the focusing strength to adjust the beam envelope. The observed dependence on g -factor is due primarily to the varying onset of the nonlinear phase and the associated final drop, larger g values corresponding to an earlier onset, and thus lower final emittance. In Fig. 11, we vary the initial beam current; it is varied together with focusing strength to keep the beam size approximately constant.

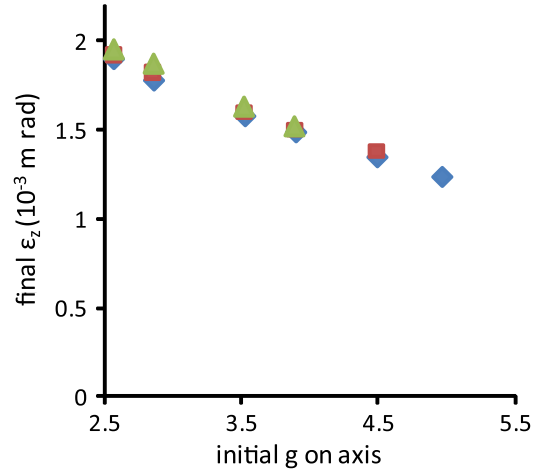


FIG. 10. Final z emittance at $z = 60$ m ($\times 10^{-3}$) vs initial geometric factor on axis with various pipe radius.

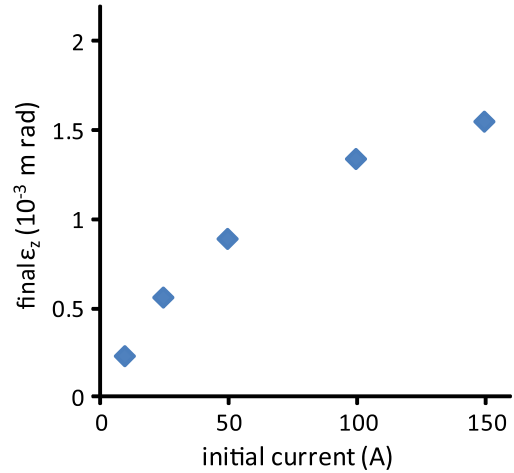


FIG. 11. Final z emittance at $z = 60$ m ($\times 10^{-3}$) vs initial peak current.

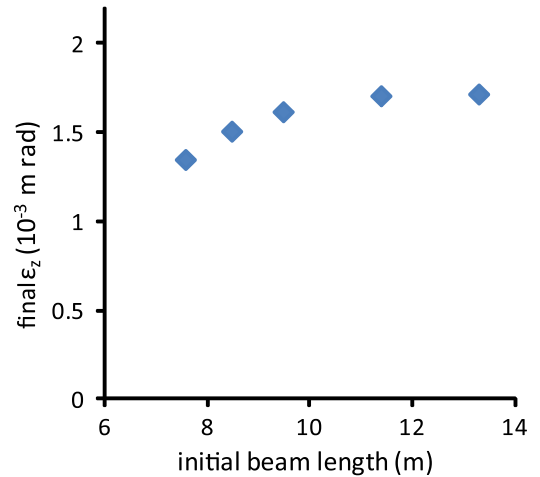


FIG. 12. Final z emittance at $z = 60$ m ($\times 10^{-3}$) vs initial edge-to-edge beam length, with fixed peak current, thus total charge scales proportionally with beam length.

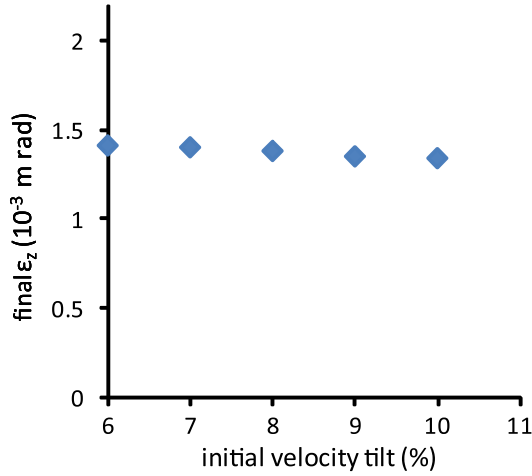


FIG. 13. Final z emittance at $z = 60$ m ($\times 10^{-3}$) vs initial velocity tilt.

Results show that the final emittance has a strong dependence on current, which is consistent with our expectation as space charge force increases linearly with current. In Fig. 12, we vary the initial beam length, while the peak current is kept constant. The total amount of charge is therefore changing with beam length. It is somewhat surprising that the growth is nearly independent of the beam length. For the shorter beams, the slightly lower final emittance is due to an earlier onset of the nonlinear phase, in contrast to the long beams which stay in the linear regime through the entire 60 meters. Lastly, we vary the amount of velocity tilt, and the result is shown in Fig. 13. We found small dependence of final emittance within the range tested.

In the above runs no bends were present. We have found that the effects of the bends are negligible in the high

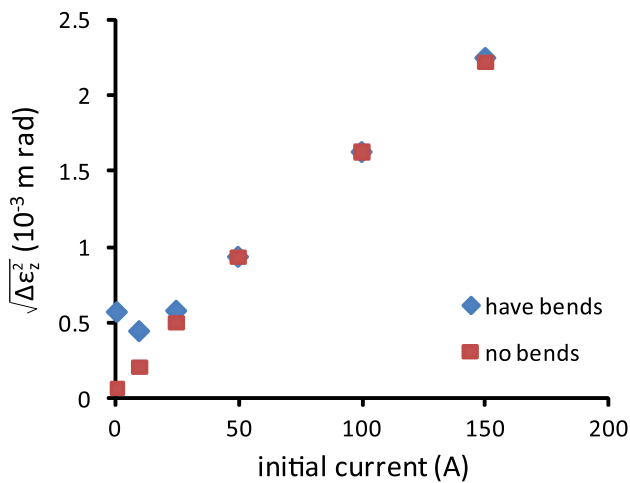


FIG. 14. Square root of $\Delta\epsilon_z^2$ as a function of initial current with nonzero initial emittance; effect of bend shows up in low current regime. Otherwise, longitudinal emittance growth is dominated by space charge.

current cases. The effects of bends show up in cases with currents less than around 30 A (see Fig. 14).

Looking at the same data at an earlier position (at $z = 20$ m), the growth is linear in all cases. At this position, the features noted become even more evident. The linear growth rate is clearly independent of g-factor, pulse length, and velocity tilt, and is linear with current. This very simple result motivated us to look for an analytic understanding, which we present in the next section. The WARP data at 20 m will be shown together with the analytic results in Figs. 16–19.

V. ANALYTIC RESULT ON LONGITUDINAL EMITTANCE GROWTH

In this section, we calculate the linear growth rate within the g-factor model. We assume a perfect parabolic line charge density and a linear initial phase space which has zero emittance. Although realistic beams have nonzero emittance, we will focus on the zero emittance case. The reason is the same as that in doing simulations, since it is for a baseline study. In addition, the same emittance can be obtained from many individual phase space profiles, each can behave differently. There is in general no unique solution in the case with nonzero initial emittance, so we stick with zero emittance, where phase space can only be straight lines. In sections below, we consider 2 ideal cases: the first case for a beam with constant beam radius from head to tail, and a second case with uniform current density throughout the entire beam. We calculate the contribution to longitudinal emittance by the nonlinear terms in g , by directly evaluating the terms from the definition of longitudinal emittance [Eq. (3)]. The ensemble average terms are calculated directly by integration, for example,

$$\langle(\Delta v_z)^2\rangle = \frac{1}{C} \int \rho(v - v_b)^2 d^3r. \tag{11}$$

C is the total charge and ρ is the volume charge density, the beam extends from $z = -L/2$ to $+L/2$. The beam starts with a perfectly linear velocity tilt with zero longitudinal temperature, i.e., zero initial longitudinal emittance.

A. Beam with uniform radius

Consider a circular beam with uniform radius along its length, with uniform cross sectional density and parabolic line density, i.e.,

$$\rho(z) = \frac{\lambda(z)}{\pi a^2} \tag{12}$$

$$\lambda(z) = \frac{3C}{2L} \left(1 - 4\frac{z^2}{L^2}\right). \tag{13}$$

Staying on axis, the longitudinal space charge force is linear. However, there is a radial dependence of g :

$$g(r) = 2 \ln\left(\frac{R_p}{a}\right) + 1 - \frac{r^2}{a^2}, \quad (14)$$

hence the electric field:

$$E_z(z, r, t) = \frac{g(r)}{4\pi\epsilon_0} \cdot 12C \frac{z}{L^3} \quad (15)$$

which leads to off axis particles experiencing smaller forces than those on axis. If particles always stay at the same distance from the axis, i.e., flow is laminar, there will be a systematic difference in force within each beam slice, which would lead to a spread in beam energy. The time dependence is hidden in L , as the beam we consider is compressing due to the given tilt. Here we take some simplifications to the problem. First, we assume the beam maintain a self-similar shape (i.e. parabolic), only its length L scales with time, hence the position parameter is $s = z/L$ rather than z . Second, within the short time interval, we assume z is not affected by E_z , by the fact that z scales with $E_z t^2$, its effect appears slower than v_z . This is also required to be consistent with the first assumption. Therefore $\langle(\Delta z)^2\rangle$ is just the mean-square length:

$$\langle(\Delta z)^2\rangle = \frac{1}{C} \int \rho z^2 d^3 r = \frac{L^2}{20}. \quad (16)$$

The third assumption is we neglect the space charge slow-down effect on beam compression, i.e., beam length only depends on the initially given tilt; in other words, beam length change linearly with time, such that

$$L(t) = L_o - v_b f t, \quad (17)$$

where L_o is the initial length and f is the initial tilt. This approximation is quite good within a short time, especially if the tilt is large.

With all these assumptions, we can now evaluate the evolution of emittance:

$$v(r, s, t) = v_b(1 + s f) + \frac{12qCg(r)}{4\pi\epsilon_0 m} s \cdot F(t) \quad (18)$$

with

$$F(t) = \int \frac{dt'}{(L_o - v_b f t')^2} = \frac{t}{L(t) \cdot L_o}. \quad (19)$$

From velocity of particles,

$$\langle(\Delta v_z)^2\rangle = \frac{1}{C} \int \rho (v - v_b)^2 d^3 r \quad (20)$$

$$= \frac{1}{C} \int \frac{3C}{2L\pi a^2} (1 - 4s^2) [v_b s f + 12ACg(r)sF(t)]^2 d^3 r \quad (21)$$

$$= \frac{12}{5} (ACF)^2 (1 - 3g_o - 3g_o^2) + \frac{3}{5} ACF(2g_o - 1)v_b f + \frac{v_b^2 f^2}{20}, \quad (22)$$

where $A = q/4\pi\epsilon_0 m$ and $g_o = 2 \ln(R_p/a) + 1$.

Similarly,

$$\langle(\Delta v_z z)\rangle = \frac{1}{C} \int \rho z (v - v_b) d^3 r \quad (23)$$

$$= \frac{L}{C} \int \frac{3C}{2L\pi a^2} (1 - 4s^2) [v_b s f + 12ACg(r)sF(t)] s d^3 r \quad (24)$$

$$= \left[\frac{3}{10} ACF(2g_o - 1) + \frac{v_b f}{20} \right] L. \quad (25)$$

Putting all terms together,

$$\epsilon_z^2 = \frac{16}{v_b^2} [\langle(\Delta z)^2\rangle \langle(\Delta v_z)^2\rangle - \langle\Delta z \Delta v_z\rangle^2] \quad (26)$$

$$= \frac{144}{300v_b^2} \left(\frac{AC}{L_o} t \right)^2. \quad (27)$$

Hence,

$$\epsilon_z = \sqrt{\frac{12}{25}} \frac{qC}{4\pi\epsilon_0 m v_b L_o} t \quad (28)$$

or

$$\epsilon_z = \sqrt{\frac{12}{25}} \frac{q^2 N}{4\pi\epsilon_0 m v_b^3 \tau_o} d \cong 0.69 \frac{q^2 N}{4\pi\epsilon_0 m v_b^3 \tau_o} d, \quad (29)$$

where N is number of ions, d is the distance traveled, and τ_o is the initial pulse duration in time. We note that the longitudinal emittance only depends on total charge/initial beam length, which is also proportional to the peak line charge density. The growth is linear with time (or distance traveled), i.e., a constant growth rate. These features agree with the simulation results from Sec. IV.

It is interesting that the emittance growth does not depend on the vacuum chamber radius and beam radius, since the space-charge force clearly depends on these parameters (evident from the g-factor model). The physical origin can be traced back to Eq. (10), where the leading term in the g-factor depends on the chamber and beam radius, but the nonlinear term, which is responsible for the emittance growth, depends only on the dimensionless parameter r/a .

B. Beam with uniform charge density

Another ideal case is a beam with uniform charge density all over its volume. This is in fact the initial condition assumed for the beams in the simulations of Sec. IV. For the same parabolic line density and cross section:

$$\rho = \frac{\lambda(z)}{\pi a^2(z)} \quad (30)$$

$$\lambda(z) = \frac{3C}{2L} \left(1 - 4 \frac{z^2}{L^2} \right). \quad (31)$$

The beam envelope can be written as a function of $s = z/L$:

$$a^2(z) = \frac{3C}{2\pi\rho L}(1 - 4s^2). \quad (32)$$

We assume g-factor still holds towards the ends of beam, which is given by

$$g(s) = 2 \ln\left(\frac{R_p}{a}\right) = \ln\left(\frac{2\pi\rho LR_p^2}{3C(1 - 4s^2)}\right). \quad (33)$$

Note that this assumption may not be really correct and that divergence occurs as s tends to $\pm 1/2$. However, as the line charge density falls off rapidly, the final result converges. As the edge contribution is small, we expect emittance calculated is well approximated.

In Eq. (29), the g-factor consists of only axial dependence, as the radial term is canceled exactly in the below expression, since ρ and, hence, λ/a^2 is constant [12]:

$$E_z = -\frac{1}{2\pi\epsilon_0} \left[\frac{1}{2} \left(1 - \frac{r^2}{a^2}\right) + \ln\left(\frac{R_p}{a}\right) \right] \frac{\partial \lambda}{\partial z} - \frac{1}{2\pi\epsilon_0} \left(1 - \frac{r^2}{a^2}\right) \frac{\lambda}{a} \frac{\partial a}{\partial z}, \quad (34)$$

where

$$\frac{\partial a}{\partial z} = \frac{a}{2\lambda} \frac{\partial \lambda}{\partial z}. \quad (35)$$

Following similar calculations as above, but replacing $g(r)$ with $g(s)$:

$$\begin{aligned} \langle (\Delta v_z)^2 \rangle &= \frac{1}{C} \int \rho (v - v_b)^2 d^3 r \\ &= \frac{4}{125} (ACF)^2 (1772 - 75\pi^2 + 930g' + 225g'^2) \\ &\quad + \frac{2}{25} ACF (15g' + 31) v_b f + \frac{v_b^2 f^2}{20}, \end{aligned} \quad (36)$$

where

$$g' = \ln\left(\frac{R_p^2}{4a_o^2}\right) = 2 \ln\left(\frac{R_p}{2a_o}\right) \quad (38)$$

$$a_o^2 = \frac{3C}{2\pi\rho L}. \quad (39)$$

Similarly,

$$\langle (\Delta v_z z) \rangle = \frac{1}{C} \int \rho z (v - v_b) d^3 r \quad (40)$$

$$= \left[\frac{1}{25} ACF (15g' + 31) + \frac{v_b f}{20} \right] L. \quad (41)$$

The final result is

$$\epsilon_z = \frac{4}{25} \sqrt{811 - 75\pi^2} \frac{qC}{4\pi\epsilon_0 m v_b L_o} t \quad (42)$$

or

$$\begin{aligned} \epsilon_z &= \frac{4}{25} \sqrt{811 - 75\pi^2} \frac{q^2 N}{4\pi\epsilon_0 m v_b^3 \tau_o} d \\ &\cong 1.35 \frac{q^2 N}{4\pi\epsilon_0 m v_b^3 \tau_o} d. \end{aligned} \quad (43)$$

The formula has the same form as the previous case with uniform envelope with just a different numerical constant. Both cases show the same dependence of longitudinal emittance growth on the initial line charge density only. We observe that the emittance growth in case A corresponds to a growth of local temperature, while case B results from a nonlinear distortion of head-to-tail beam profile. In case B, the phase space is still a thin line with no area, so the area is not directly related to emittance like common understanding (as that in case A). It seems the rms definition of emittance here does not accurately reflect thermal spread in velocity. However, the distorted beam will not converge to a single point on the target although it has no occupied phase space area. So the rms emittance rather than the phase space area is ultimately the parameter that is directly related to the pulse length at target. Figure 15 is a schematic illustration of the evolution of the longitudinal phase spaces in these two ideal cases.



FIG. 15. Longitudinal phase space (v_z vs z) evolution for the ideal cases. Top—initial phase space for both two cases, with linear tilt and no temperature. Middle—uniform radius case showing increase in thickness of the phase space as a growth of temperature. Bottom—uniform density case showing a head-to-tail distortion (S-ing) results in a growth of effective area.

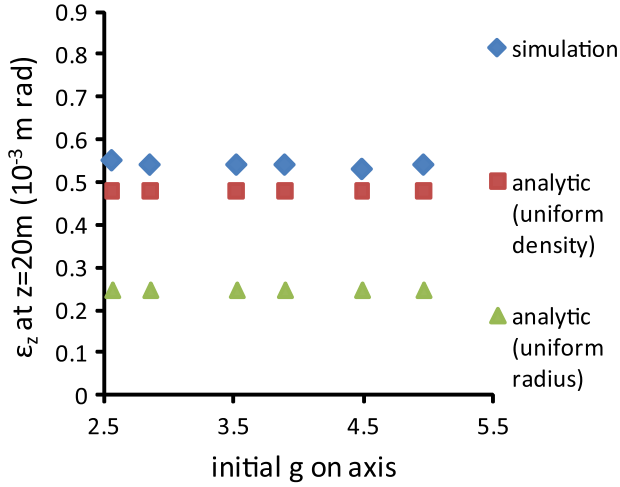


FIG. 16. z emittance at $z = 20$ m ($\times 10^{-3}$) vs initial geometric factor on axis, showing 2 cases with uniform beam radius (red), uniform charge density (green), and WARP simulation (blue).

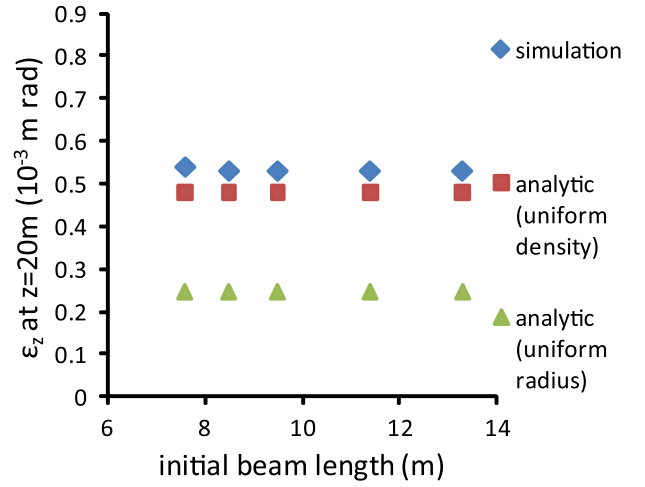


FIG. 18. z emittance at $z = 20$ m ($\times 10^{-3}$) vs initial beam length with fixed peak current, showing 2 cases with uniform beam radius (green), uniform charge density (red), and WARP simulation (blue).

C. Comparison of analytic formula with WARP simulation

We take the WARP simulation results and compare with the derived formula; the longitudinal emittance values at $z = 20$ m are plotted as functions of initial parameters (Figs. 16–19). The derived and simulated growth with canonical parameters is plotted as a function of distance as well (Fig. 20). Both results show that initial growth rate of ϵ_z is proportional to initial current but independent of the other 3 parameters. The prediction of the uniform charge density case is well matched to the simulations in terms of the initial growth rate, except for the ripples

related to quadrupole focusing. This is expected as the beam in the WARP simulation is initialized with the assumptions of case B. For more general beams intermediate between the cases considered above, it is expected that both axial and radial nonlinearities will appear, and the final result will also have the same form as above, with different numerical factors depending on details of the initial beam profile. We can write a more general formula as

$$\epsilon_z = k \frac{q^2 N}{4\pi\epsilon_o m v_b^3 \tau_o} d. \quad (44)$$

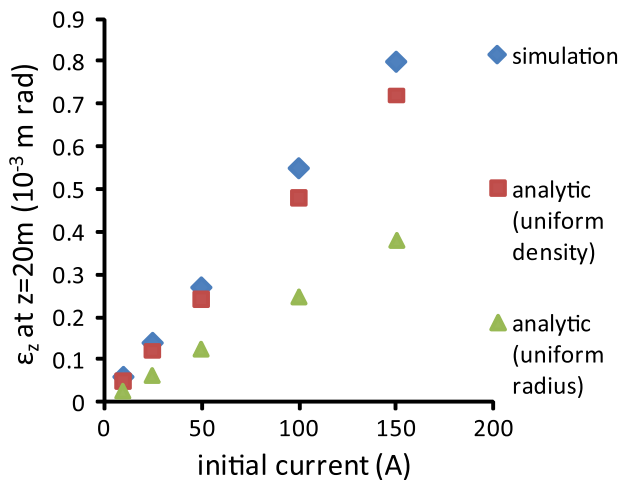


FIG. 17. z emittance at $z = 20$ m ($\times 10^{-3}$) vs initial current, showing 2 cases with uniform beam radius (green), uniform charge density (red), and WARP simulation (blue).

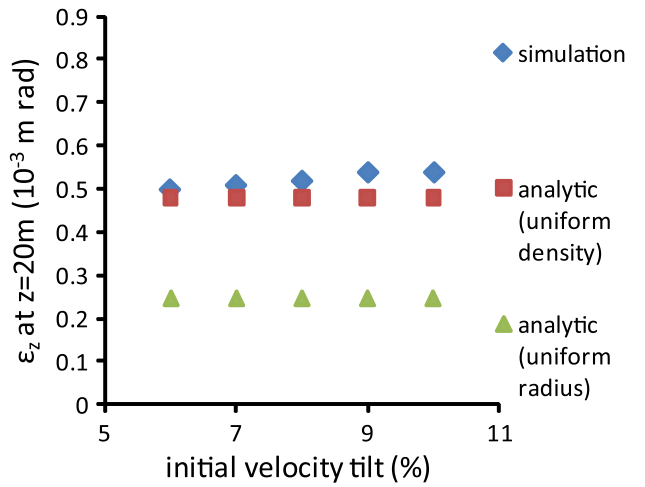


FIG. 19. z emittance at $z = 20$ m ($\times 10^{-3}$) vs initial tilt, showing 2 cases with uniform beam radius (green), uniform charge density (red), and WARP simulation (blue).

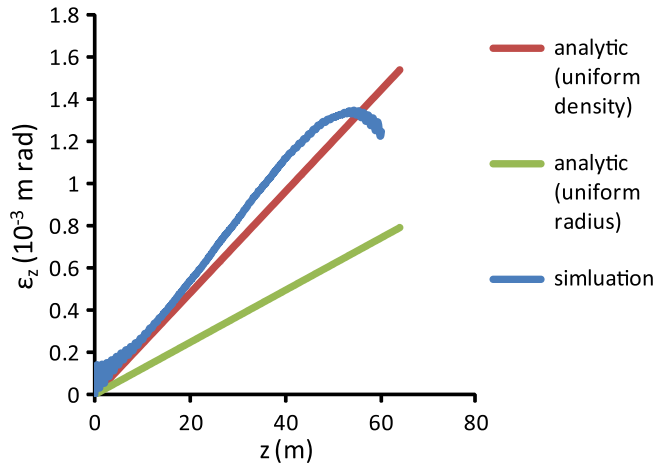


FIG. 20. z emittance vs z (m), showing 2 cases with uniform beam radius (green), uniform charge density (red), and WARP simulation (blue).

Here k is the numerical factor to be determined. For the two cases discussed above, k has values of order unity.

VI. CONCLUSIONS

Longitudinal emittance is a limiting factor to the final pulse length. In many driver designs where bends are present, it also induces transverse emittance growth and in turn enlarges the spot size on target. Both of them are crucial requirements in heavy ion fusion applications. We present in this paper one mechanism for longitudinal emittance growth, due to self-nonlinear space-charge force. The growth is proportional to line charge density and distance traveled. It suggests that the growth can be reduced by designing beam lines with short drift distance and separating high current beams into multiple beamlets, when short pulses are required. Another important question is whether the emittance growth described in this paper can be reversed or mitigated, either by external means or by inherent mechanisms. We observe that in the case of uniform charge density (case B), the emittance growth mainly results from a head-to-tail distortion of the longitudinal phase space (it takes an “S” shape). This emittance can be reduced if the distortion is corrected, for example, by correction voltage pulses with just the right form to undo

the S-ing. This method becomes prohibitively costly if applied to individual beams in each of the drift compression beam lines, where they are separated. A second possible way is to prepare the beam bundle before the exit of the accelerator with a head-to-tail energy profile to compensate in advance the nonlinear distortion in the drift compression section. Finally, we observed in our simulations a significant drop in the longitudinal emittance as we move beyond the region of linear growth. We observe that the phase space distortions undo themselves to a certain extent. We are exploring all of these mechanisms for the reduction of longitudinal emittance.

- [1] E.P. Lee and J.J. Barnard, *Laser Part. Beams* **20**, 581 (2002) [<http://escholarship.org/uc/item/8xj0z1mh>].
- [2] D.P. Grote, A. Friedman, J.L. Vay, and I. Haber, *AIP Conf. Proc.* **749**, 55 (2005).
- [3] W.M. Sharp, A. Friedman, and D.P. Grote, *Fusion Eng. Des.* **201**, 32 (1996) [<http://www.osti.gov/bridge/purl.cover.jsp?purl=/192508-UbT7Xj/webviewable/>].
- [4] S. Koscielniak, in *Proceedings of the 19th Particle Accelerator Conference, Chicago, Illinois, 2001* (IEEE, Piscataway, NJ, 2001), pp. 2970–2972.
- [5] R. Baartman, “Form factor g in longitudinal space charge impedance”, internal note, 1992 (unpublished).
- [6] Y.Y. Lau, S.S. Yu, J.J. Barnard, and P.A. Seidl (unpublished).
- [7] J. Runge and B.G. Logan, *Phys. Plasmas* **16**, 033109 (2009).
- [8] P.K. Roy, S.S. Yu, E. Henestroza, A. Anders, F.M. Bieniosek, J. Coleman, S. Eylon, W.G. Greenway, M. Leitner, B.G. Logan, W.L. Waldron, D.R. Welch, C. Thoma, A.B. Sefkow, E.P. Gilson, P.C. Efthimion, and R.C. Davidson, *Phys. Rev. Lett.* **95**, 234801 (2005).
- [9] Y.J. Chen, Lawrence Livermore National Laboratory Technical Report, 2003.
- [10] D. Neuffer, Fermi National Accelerator Lab Technical Report, 1997.
- [11] J.J. Barnard, H.D. Shay, S.S. Yu, A. Friedman, and D.P. Grote, in *Proceedings of the 1992 Linear Accelerator Conference (AECL Research, Ottawa, Canada, 1992)*.
- [12] J.J. Barnard and K. Horioka, *Induction Accelerators* (Springer, Berlin, 2011), Chap. 9.